Journal of Computational Physics **150,** 17–39 (1999)
Article ID jcph.1998.6162, available online at http://www.idealibrary.com on IDEAL®

Low-Speed Flow Simulation by the Gas-Kinetic Scheme

Mingde Su,* Kun Xu,† and M. S. Ghidaoui‡

*Department of Engineering Mechanics, Tsinghua University, Beijing, 100084, People's Republic of China; and †Mathematics Department and ‡Department of Civil Engineering, Hong Kong University of Science and Technology, Clear Water Bay, Kowloon, Hong Kong
E-mail: *sumd@mail.tsinghua.edu.cn, †makxu@uxmail.ust.hk, and ‡ghidaoui@usthk.ust.hk

Received June 30, 1998; revised December 3, 1998

This paper extends the gas-kinetic BGK-type scheme to low Mach number flows, and thus shows that incompressible flow solutions are accurately obtained from the BGK scheme in the low Mach number limit. The influence of boundary conditions, internal molecular degrees of freedom K, and the flow Mach number M on the accuracy of the solutions of incompressible or nearly incompressible flow problems is quantitatively evaluated. The gas-kinetic scheme is tested carefully in two numerical examples, namely, the cavity flow problem and the flow passing a backward facing step problem. For the cavity flow problem, the numerical results from the gas-kinetic scheme under different Reynolds numbers compare well with Ghia's data. For the backward step problem, the numerical results are compared accurately with previously published experimental data.

Key Words: low-speed flow; kinetic scheme; incompressible Navier–Stokes equations.

1. INTRODUCTION

Great progress has been achieved in the field of computational fluid dynamics of incompressible flows in the past few decades [4, 7]. Despite this success, there remain two main challenges in the numerical solutions of incompressible fluid flows. First, the incompressible flow assumption eliminates the unsteady term from the continuity equation and reduces the mass conservation equation to a divergence free velocity field. Therefore, the absence of density from the incompressible fluid flow equations decouples the continuity equation from the momentum and energy equations. Hence, the divergence free velocity field becomes an implicit condition for solving the momentum and energy equations. The enforcement of the divergence free velocity field condition requires the solution of Poisson's equation for the pressure field. However, for complicated geometry, the Poisson solver is the most time consuming part in the whole flow calculations. The second challenge in the solution of

0021-9991/99 $30.00

incompressible fluid flow equations relates to the proper choice of intermediate boundary conditions [6]. In fact, Ref. [6] provides excellent insight into the problems associated with some intermediate boundary conditions and shows which intermediate boundary is optimal for viscous incompressible flows.

Conceptually, it seems plausible that the problems associated with the solution of the Poisson equation and the boundary conditions in incompressible flows can be avoided by applying compressible flow codes to problems where flow Mach number tends to zero. However, the extention of a compressible code to incompressible limit is not straightforward and can be problematic. For example, the large disparity between the speed of acoustic waves and the speed of convective waves which occurs whenever the flow Mach number approaches zero causes inaccuracy and stability problems for conventional flux-splitting methods that are based on the exact or approximate Riemann solvers, such as Roe, van Leer, Osher, and AUSM splitting [10]. In fact, singularities exist in all these flux splitting methods when $M \to 0$. This is not surprising given that a proper formulation of a numerical technique for the compressible flow equations requires an upwinding procedure, thus implying a finite wave speed (i.e., $M \neq 0$).

A possible approach to dealing with the problem of singularity encountered when applying a compressible code to model a small Mach number flow is to redefine the "representative" sound speed c when the flow Mach number becomes smaller than a specified threshold (e.g., 0.3) [15]. Some approaches are based on discarding the energy equation for the compressible fluid [5], and the gas is considered as barotropic, such as those with equal temperature. In recent years, the lattice Boltzmann method has been successfully applied to incompressible, isothermal flows [8]. However, due to the specific discretization of particle velocities in the phase space, the lattice Boltzmann method still has difficulties in compressible flow limit and maintaining the correct energy equation [2].

The development of gas-kinetic schemes has attracted much attention in recent years. These schemes are based on the approximate collisional Boltzmann equation, such as the BGK model [1]. The resulting numerical models are often referred to as collisional BGK schemes for the compressible Euler and Navier–Stokes equations [14]. A complete description of the BGK scheme can be found in a recent lecture note [12]. Unlike upwind schemes, such as those based on Riemann solvers, the BGK method is basically solving the viscous equations, where the dissipation is controlled by the particle collision time. The objective of this paper is to simplify the original BGK method in the smooth flow region and extend it to the low Mach number flows.

The paper is organized as follows. In Section 1, the BGK scheme for the low-speed flow is presented. In Section 2, the scheme is applied to the 2D cavity flow calculation and the results are compared with Ghia's data. The agreement between both results is extraordinary. The origin of the errors from the boundary condition, the molecule's internal degree of freedom, and the Mach number M are presented in detail in Section 3. In Section 4, the kinetic scheme is applied to the flow over a backward facing step problem. Numerical examples validate the current scheme for the solutions of low-speed flow. The last section provides the conclusions.

2. BGK SCHEME IN LOW-SPEED LIMIT

The BGK model in two-dimensional case is

$$f_t + u f_x + v f_y = \frac{g - f}{\tau}, \tag{1}$$

where f is the real gas distribution function and g is the equilibrium state approached by f. Both f and g are functions of space x, y; time t; particle velocity u, v; and internal degrees of freedom ξ. The particle collision time τ is related to viscosity coefficient, which depends on the local macroscopic flow variables, such as temperature.

The equilibrium state g in the 2D BGK model has the form

$$g = \rho\left(\frac{\lambda}{\pi}\right)^{(K+2)/2} e^{-\lambda[(u-U)^2+(v-V)^2+\xi^2]}, \tag{2}$$

where ρ is density, U and V are the macroscopic velocities in x and y directions, and λ is a function of temperature $\lambda = m/2kT$. ξ is a vector in K dimensions (not necessarily an integer) and ξ^2 is

$$\xi^2 = \xi_1^2 + \xi_2^2 + \cdots + \xi_K^2.$$

In D dimensions, K is related to the specific heat ratio γ through the relation [12]

$$\gamma = \frac{K + D + 2}{K + D},$$

where D is the number of dimensions.

The connection between mass ρ, momentum $\rho U (= m)$, $\rho V (= n)$, and energy $\rho\epsilon$ densities and the distribution function f is

$$W = \begin{pmatrix} \rho \\ \rho U \\ \rho V \\ \rho\epsilon \end{pmatrix} = \begin{pmatrix} \rho \\ m \\ n \\ \rho\epsilon \end{pmatrix} = \int \psi_\alpha f \, du \, dv \, d\xi, \qquad \alpha = 1, 2, 3, 4, \tag{3}$$

where $d\xi = d\xi_1 \, d\xi_2 \cdots d\xi_K$, ψ_α is the vector

$$\psi_\alpha = \left(1, u, v, \frac{1}{2}(u^2 + v^2 + \xi^2)\right)^T, \tag{4}$$

and $du \, dv \, d\xi$ is the volume element in the phase space. Since mass, momentum, and energy are conserved during particle collisions, f and g must satisfy the conservation constraint

$$\int (g - f)\psi_\alpha \, du \, dv \, d\xi = 0, \qquad \alpha = 1, 2, 3, 4, \tag{5}$$

at any point in space and time. The fluxes for the corresponding macroscopic variables in the x-direction are

$$F(W) = \begin{pmatrix} F_\rho \\ F_m \\ F_n \\ F_{\rho\epsilon} \end{pmatrix} = \int u\psi_\alpha f \, du \, dv \, d\xi. \tag{6}$$

From Eq. (1), the compressible Navier–Stokes equations can be derived, where the shear stress tensor can be expressed as

$$\sigma_{ij} = \eta\left[\left(\frac{\partial U_i}{\partial x_j} + \frac{\partial U_j}{\partial x_i} - \delta_{ij}\frac{\partial U_k}{\partial x_k}\right) + \frac{K}{K+2}\delta_{ij}\frac{\partial U_k}{\partial x_k}\right], \tag{7}$$

where dynamic viscosity coefficient is

$$\eta = \tau p,$$

and the second viscosity coefficient becomes

$$\varsigma = \frac{K}{K+2}\tau p.$$

In the above equations, p is the local fluid pressure with the relation $p = \rho/2\lambda$. The second viscosity coefficient is solely related to the internal degree of freedom through the compressibility of the fluid, which can be totally eliminated by the choice of $K = 0$, which corresponds to $\gamma = 2$ in the 2D case.

In order to develop a finite volume gas-kinetic scheme, take moments of ψ_α in Eq. (1) and integrate them with respect to $du\,dv\,d\xi$ in phase space, $dx\,dy$ in a numerical cell $[x_{i-1/2,j}, x_{i+1/2,j}] \times [y_{i,j-1/2}, y_{i,j+1/2}]$, and time dt in a time step $[t^n, t^{n+1}]$,

$$\int (f_t + uf_x + vf_y)\psi_\alpha\,du\,dv\,d\xi\,dx\,dy\,dt = \int \frac{g-f}{\tau}\psi_\alpha\,du\,dv\,d\xi\,dx\,dy\,dt;$$

with conditions (3), (5), and (6), we can get

$$W_{i,j}^{n+1} - W_{i,j}^{n} = \frac{1}{\Delta S_{i,j}} \sum_{k=1}^{k=4} \int_0^{\Delta t} \vec{F}_k \cdot \vec{l}_k\,dt, \tag{8}$$

where $\Delta t = t^{n+1} - t^n$, and $\vec{F}$ is the flux across cell interfaces, which can be obtained from the integration of the particle distribution function. $\Delta S_{i,j}$ is the area of the numerical cell (i, j) and $|\vec{l}_k|$ the length of the cell interface with the normal direction $\vec{k}$.

Since the BGK model is solved in the current paper by using a directional splitting scheme, in what follows we only present the numerical discretization for the fluxes in the x-direction; a similar formula can be found in the y-direction. In the x-direction, the BGK model can be reduced to

$$f_t + uf_x = \frac{g-f}{\tau}. \tag{9}$$

For subsonic flow without shocks, the general solution of f for the above equation at the cell interface $x_{i+1/2}$ and time t can be simplified as [11]

$$f(x_{i+1/2}, t, u, v, \xi) = \frac{1}{\tau}\int_{-\infty}^{t} g(x', t', u, v, \xi)e^{-(t-t')/\tau}\,dt', \tag{10}$$

where $x' = x_{i+1/2} - u(t-t')$ is the trajectory of a particle motion. Generally, the equilibrium state g around the cell interface $x_{i+1/2}$ at the beginning of each time step $t = 0$ is assumed to be

$$g(x, t, u, v, \xi) = g_0(1 + a(x - x_{i+1/2}) + At), \tag{11}$$

where g_0 is the local Maxwellian located at the cell interface,

$$g_0 = \rho_0\left(\frac{\lambda_0}{\pi}\right)^{(K+2)/2} e^{-\lambda_0[(u-U_0)^2+(v-V_0)^2+\xi^2]}. \tag{12}$$

The dependence of a, A in Eq. (11) on the particle velocities can be obtained from the Taylor expansion of a Maxwellian and have the forms of

$$a = a_1 + a_2 u + a_3 v + a_4 \frac{1}{2}(u^2 + v^2 + \xi^2) = a_\alpha \psi_\alpha,$$
$$A = A_1 + A_2 u + A_3 v + A_4 \frac{1}{2}(u^2 + v^2 + \xi^2) = A_\alpha \psi_\alpha,$$

where all coefficients of $a_1, a_2, \ldots, A_4$ are local constants.

For the low-speed flow, at the beginning of each time step $t = 0$, the values of macroscopic variables on the cell interfaces and their slopes in the normal direction can be calculated from the discretized initial data W_i. In the present paper, a third-order accurate interpolation scheme is used, and the macroscopic variables at the cell interface and their slopes are constructed as

$$W_{i+1/2} = \frac{7}{12}(W_i + W_{i+1}) - \frac{1}{12}(W_{i-1} + W_{i+2}), \tag{13}$$

$$\left(\frac{dW}{dx}\right)_{i+1/2} = \left(\frac{5}{4}(W_{i+1} - W_i) - \frac{1}{12}(W_{i+2} - W_{i-1})\right) \Big/ \Delta x, \tag{14}$$

where Δx is the cell size. With the above macroscopic distributions, the microscopic gas distribution function g at time $t = 0$ can be determined:

$$\int \psi_\alpha g_0 \, du \, dv \, d\xi = W_{i+1/2} = \begin{pmatrix} \rho \\ \rho U \\ \rho V \\ \rho \epsilon \end{pmatrix}_{i+1/2}$$

and

$$\int a \psi_\alpha g_0 \, du \, dv \, d\xi = \left(\frac{dW}{dx}\right)_{i+1/2}.$$

The parameters in the Maxwellian distributions g_0 in Eq. (12) are

$$\begin{pmatrix} \rho_0 \\ U_0 \\ V_0 \\ \lambda_0 \end{pmatrix} = \begin{pmatrix} \rho \\ U \\ V \\ \frac{(K+2)\rho}{4\left(\rho\epsilon - \frac{1}{2}(m^2+n^2)/\rho\right)} \end{pmatrix}_{i+1/2}. \tag{15}$$

After determining g_0 in the above equations, we can find a from the slopes of macroscopic variables across a cell interface

$$\frac{1}{\rho_0}\left(\frac{dW}{dx}\right)_{i+1/2} \equiv \begin{pmatrix} \Delta\rho \\ \Delta m \\ \Delta n \\ \Delta\rho\epsilon \end{pmatrix} = M_{\alpha\beta} \begin{pmatrix} a_1 \\ a_2 \\ a_3 \\ a_4 \end{pmatrix} = M_{\alpha\beta} a_\beta, \tag{16}$$

where the matrix $M_{\alpha\beta} = 1/\rho_0 \int g_0 \psi_\alpha \psi_\beta \, du \, dv \, d\xi$ is

$$M_{\alpha\beta} = \begin{pmatrix} 1 & U_0 & V_0 & \mathcal{B}_1 \\ U_0 & U_0^2 + 1/2\lambda_0 & U_0 V_0 & \mathcal{B}_2 \\ V_0 & U_0 V_0 & V_0^2 + 1/2\lambda_0 & \mathcal{B}_3 \\ \mathcal{B}_1 & \mathcal{B}_2 & \mathcal{B}_3 & \mathcal{B}_4 \end{pmatrix}, \tag{17}$$

and

$$\mathcal{B}_1 = \frac{1}{2}\big(U_0^2 + V_0^2 + (K+2)/2\lambda_0\big),$$
$$\mathcal{B}_2 = \frac{1}{2}\big(U_0^3 + V_0^2 U_0 + (K+4)U_0/2\lambda_0\big),$$
$$\mathcal{B}_3 = \frac{1}{2}\big(V_0^3 + U_0^2 V_0 + (K+4)V_0/2\lambda_0\big),$$

and

$$\mathcal{B}_4 = \frac{1}{4}\big(\big(U_0^2 + V_0^2\big)^2 + (K+4)\big(U_0^2 + V_0^2\big)/\lambda_0 + (K^2 + 6K + 8)/4\lambda_0^2\big).$$

The above matrix can be easily inverted, and the solutions for a in Eq. (16) can be expressed as

$$a_4 = \frac{4\lambda_0^2}{K+2}(2\Delta\epsilon - 2U_0\Delta U - 2V_0\Delta V),$$
$$a_3 = 2\lambda_0\left(\Delta V - \frac{V_0}{2\lambda_0}a_4\right),$$
$$a_2 = 2\lambda_0\left(\Delta U - \frac{U_0}{2\lambda_0}a_4\right),$$
$$a_1 = \frac{1}{\rho_0}\Delta\rho - U_0 a_2 - V_0 a_3 - \frac{1}{2}\left(U_0^2 + V_0^2 + \frac{K+2}{2\lambda_0}\right)a_4,$$

where

$$\Delta U = (\Delta m - U_0\Delta\rho),$$
$$\Delta V = (\Delta n - V_0\Delta\rho),$$
$$\Delta\epsilon = \left(\Delta(\rho\epsilon) - \frac{1}{2}\left(U_0^2 + V_0^2 + \frac{K+2}{2\lambda_0}\right)\Delta\rho\right).$$

After substituting Eq. (11) into Eq. (10), the final gas distribution function at a cell interface is

$$f(x_{i+1/2}, t, u, v, \xi) = g_0(1 - \tau u a + (t - \tau)A); \tag{18}$$

the only unknown in the above equation is A. Since

$$g(x_{i+1/2}, t, u, \xi) = g_0(1 + At),$$

and with the compatibility condition

$$\int \psi_\alpha (f - g)\, du\, dv\, d\xi = 0,$$

along the time t and at $x = x_{i+1/2}$, A can be uniquely determined from

$$\int (ua + A)\psi_\alpha g_0\, du\, dv\, d\xi = 0,$$

which gives

$$M_{\alpha\beta} A_\beta = -\frac{1}{\rho_0} \int u a g_0 \psi_\alpha\, du\, dv\, d\xi, \tag{19}$$

where $M_{\alpha\beta}$ is given in Eq. (17), and the right-hand side in the above equation is known. Therefore, the above equation can be solved to obtain $A_\beta = (A_1, A_2, A_3, A_4)^T$ as that solving Eq. (16). The integrating moments of Maxwellian distribution can be found in the Appendix.

Finally, the time-dependent numerical fluxes in the x-direction across the cell interface can be computed as

$$\begin{pmatrix} \mathcal{F}_\rho \\ \mathcal{F}_m \\ \mathcal{F}_n \\ \mathcal{F}_{\rho\epsilon} \end{pmatrix}_{i+1/2} = \int u \begin{pmatrix} 1 \\ u \\ v \\ \frac{1}{2}(u^2 + v^2 + \xi^2) \end{pmatrix} g_0 (1 + \tau a u + (t - \tau) A)\, du\, dv\, d\xi. \tag{20}$$

By integrating the above equation to the whole time step Δt, we get the total mass, momentum, and energy transport. Again, the moments of a Maxwellian can be found in the Appendix. The collision time τ in the above flux functions is related to the viscosity coefficient ν through the relation

$$\nu = \frac{\tau p}{\rho}.$$

For any physical problem, with given Reynolds number Re,

$$\mathrm{Re} = \frac{UL}{\nu} = \frac{UL\rho}{\tau p},$$

we can have

$$\tau = \frac{2\lambda UL}{\mathrm{Re}},$$

where λ takes the value λ_0 in Eq. (15) and the relation $p = \rho/2\lambda$ has been used.

Remark. The time step Δt used in the above scheme is based on the CFL condition and the CFL number taken is around 0.65. For any practical simulations, the ratio between Δt and the particle collision time τ is about $\Delta t/\tau \sim 10$–100. Mathematically the scheme can be used in the limit of $\Delta t/\tau \sim 1$. However, physically the limit $\Delta t \sim \tau$ implies rarefied gas flow, and the assumption of Maxwellian and the expansion of Maxwellian in the current scheme are not valid.

3. SIMULATION OF CAVITY FLOW

In this section, the 2-D viscous flow in a cavity is simulated. In this problem, the fluid is bounded by a square and is driven by a uniform translation of the top. The cavity case shows rich vortex phenomena at many scales depending on the Reynolds number Re, and there are abundant papers in the literature to study the flow configuration. The cavity problem is an ideal test case for numerical methods devised to solve the Navier–Stokes equations because the solution of this problem displays a well-studied flow pattern.

The lack of an exact solution to the cavity flow problem means that an existing accurate and comprehensive numerical solution for this problem can be used as a benchmark to evaluate the results obtained by the proposed BGK method. Ghia *et al*. [7] obtained numerical solutions up to Re = 10,000 with 257×257 grid points by using a vorticity-stream function formulation. To date, this work is probably the most comprehensive study of the cavity flow. Therefore, the simulation results of the cavity problem by the BGK model are compared to Ghia's data. The effects of the compressibility, boundary conditions, Mach number M, internal degree of freedom K, Reynolds number Re, and grid size on the results of the BGK scheme are tested and analyzed in this section. In addition, the optimum choice for the parameters M, K, and Re are suggested and physical explanations for this choice are provided.

3.1. *Description of the Numerical Results*

In the present simulation, Cartesian coordinates are used. The top boundary moves from left to right with velocity U. A uniform mesh of 128×128 cells is used for the calculation for Re = 100, 400, 1000, 2000, 3200, and 5000, and a mesh of 256×256 is used for Re = 7500 and 10,000, respectively. The Reynolds number is defined as $\mathrm{Re} = UL/\nu$, where L is length of cavity side which is equal to 1 in this case and ν is kinematic viscosity $\nu = \eta/\rho$.

In the present computation, the velocity field at $t = 0$ (i.e., initial condition) is zero everywhere inside the cavity. To check the convergence of the BGK solution to steady state, the velocity fields at different output times t are compared. It is found that there is little differences between the results at $t = 30$ and $t = 40$ when $\mathrm{Re} \leq 5000$. However, as the Reynolds number is increased beyond 5000 (i.e., $\mathrm{Re} \geq 5000$) the simulation time t required for convergence is more than 50. The computation indicates that the increase of t with Re is rapid. When $\mathrm{Re} \gg 5000$ and with a mesh of 128×128 cells, the convergence to steady state is either slow or simply not achievable. To resolve this problem, a smaller mesh size is required. For instance, the computation shows that by increasing the number of cells to 256×256, convergence to steady state is achieved for all $\mathrm{Re} \leq 10{,}000$. To test the influence of the cell size on the accuracy of the converged solution, the results obtained with 128×128 and 256×256 are compared for Re = 1000, $K = 0$, and $M = 0.15$. This comparison shows little difference in this case (see Tables 2 and 3).

To obtain vorticities from the solution of velocity field at output time, a standard second-order central difference scheme is used to discretize the expression

$$\omega = \frac{\partial V}{\partial x} - \frac{\partial U}{\partial y}.$$

Then, the stream function is obtained by solving Poisson's equation

$$\Delta \psi = -\omega.$$

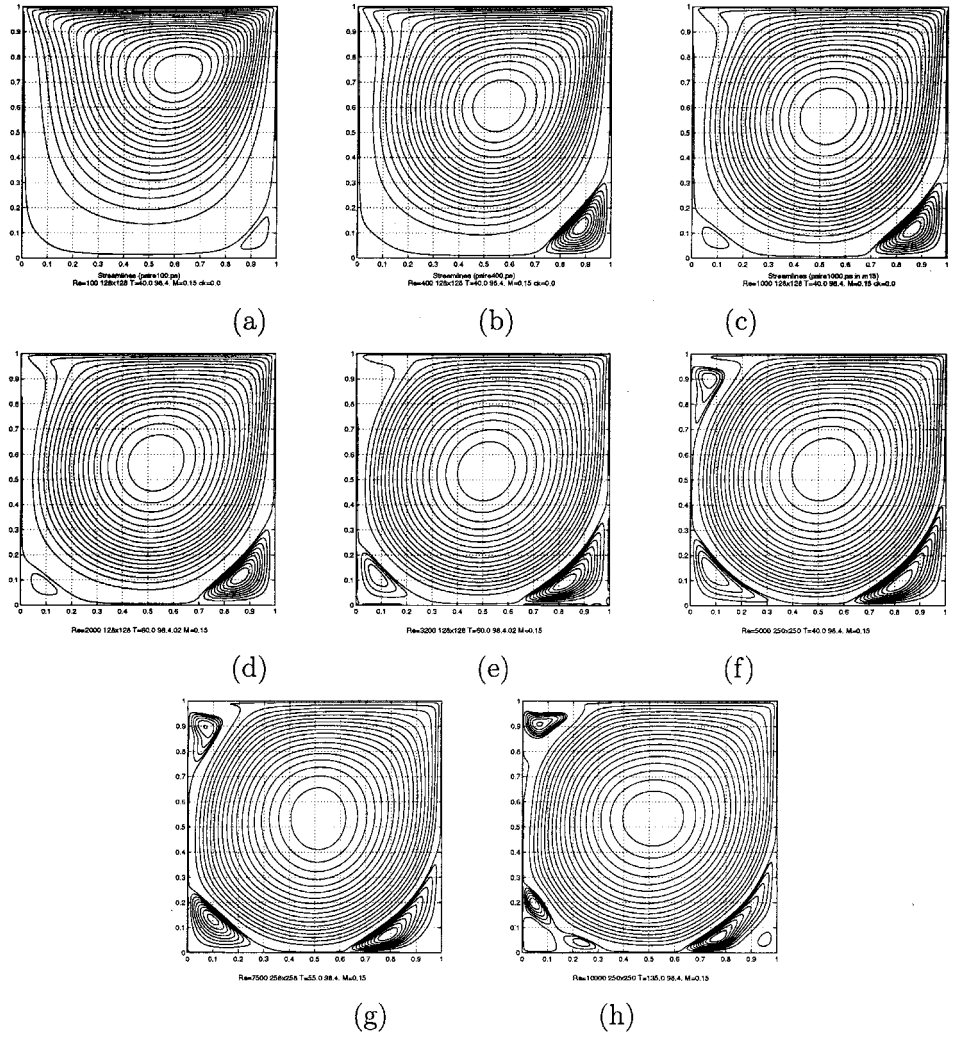

FIG. 1. Streamlines for the calculations with $K = 0$, $M = 0.15$, and (a) Re = 100; (b) Re = 400; (c) Re = 1000; (d) Re = 2000; (e) Re = 3200; (f) Re = 5000; (g) Re = 7500; (h) Re = 10,000.

The results for $K = 0$ and $M = 0.15$ are shown in Figures 1, 2, 3, and in the Tables. Figure 1 shows streamlines for different Reynolds numbers. It is apparent that the flow structure is in good agreement with that of Ghia. The effect of the Reynolds number on the flow pattern and the structure of the steady recirculating eddies in the cavity are clearly observed. Figure 2 shows the vorticity distribution inside the cavity. It is obvious that the scale of the central main vortex increases with the Reynolds number; at the same time the magnitude of the vorticity in the central region becomes larger. In Table 1, the locations of the vortex center are listed and compared with Ghia's simulation results. The relative error between the two solutions is less than 5%. The horizontal and vertical components of the U and V velocities along their respective center line are displayed in Fig. 3 for different values of Reynolds number, where the circles represent Ghia's data and the solid lines are the results obtained from the current scheme. Tables 4 and 5 list the detailed numerical data

TABLE 1
Locations of Vortex Center under Different Re Number, Where $M = 0.15$ and $K = 0$ Are Used in the Simulation

Re:	100	400	1,000	2,000	3,200	5,000	7,500	10,000
x (Ghia's):	0.62	0.56	0.54	—	—	0.52	0.51	0.51
x (present):	0.62	0.56	0.54	0.53	0.52	0.52	0.52	0.51
y (Ghia's):	0.73	0.61	0.56	—	—	0.54	0.54	0.51
y (present):	0.74	0.62	0.57	0.57	0.55	0.54	0.53	0.52

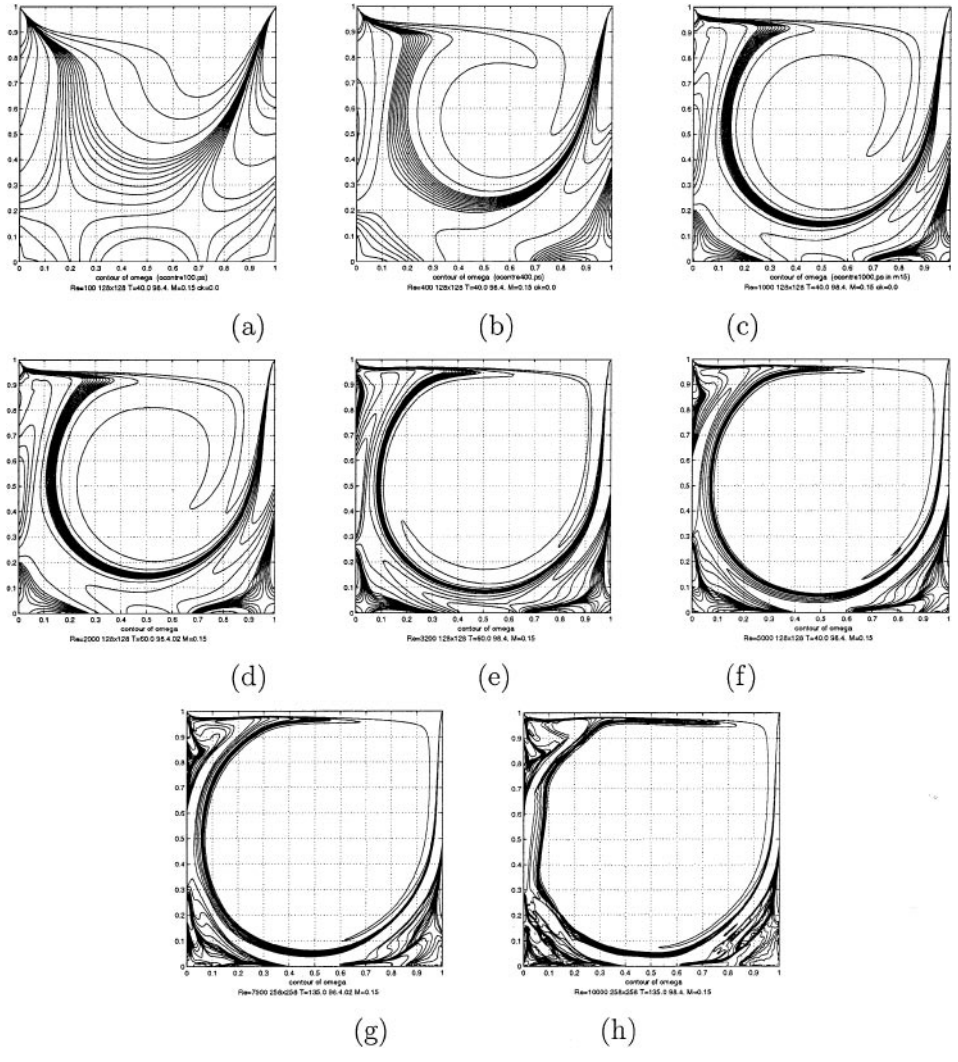

FIG. 2. Vorticity distributions for the calculations with $K = 0$, $M = 0.15$, and (a) Re = 100; (b) Re = 400; (c) Re = 1000; (d) Re = 2000; (e) Re = 3200; (f) Re = 5000; (g) Re = 7500; (h) Re = 10,000.

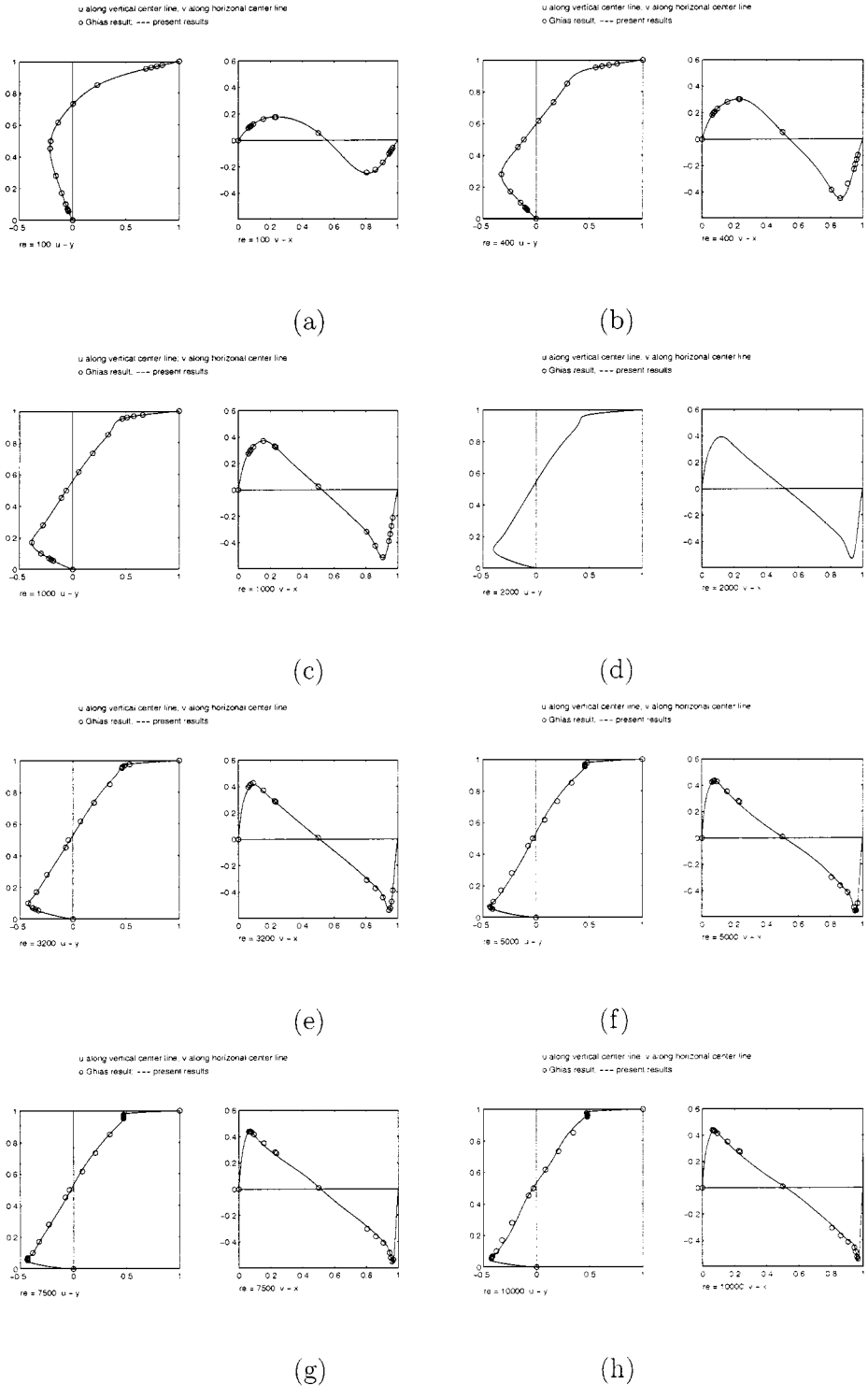

FIG. 3. U (left) and V (right) velocity distributions along vertical and horizontal lines for the calculations with $K = 0$, $M = 0.15$, and (a) Re = 100; (b) Re = 400; (c) Re = 1000; (d) Re = 2000; (e) Re = 3200; (f) Re = 5000; (g) Re = 7500; (h) Re = 10,000. (○) Ghia's data; (—) BGK results.

TABLE 2
Distribution of *U*-Velocity along Vertical Central Line with Re = 1000, *M* = 0.15, *K* = 0

y	Ghia's	*U* (128 × 128)	*U* (258 × 258)
0.00000	0.00000	0.00000	0.00000
0.05469	−0.18109	−0.17707	−0.18111
0.06250	−0.20196	−0.19798	−0.20220
0.07031	−0.22220	−0.21849	−0.22279
0.10156	−0.29730	−0.29583	−0.30026
0.17188	−0.38289	−0.38469	−0.38755
0.28125	−0.27805	−0.27824	−0.27920
0.45313	−0.10648	−0.10709	−0.10742
0.50000	−0.06080	−0.06142	−0.06150
0.61719	0.05702	0.05657	0.05706
0.73438	0.18719	0.18684	0.18809
0.85156	0.33304	0.33331	0.33591
0.95313	0.46604	0.46751	0.47056
0.96094	0.51117	0.51237	0.51528
0.96875	0.57492	0.57579	0.57855
0.97656	0.65928	0.65963	0.66252
1.00000	1.00000	1.00000	1.00000

TABLE 3
Distribution of *V*-Velocity along Horizontal Central Line with Re = 1000, *M* = 0.15, *K* = 0

x	Ghia's	*V* (128 × 128)	*V* (258 × 258)
0.0000	0.00000	0.00000	0.00000
0.0625	0.27485	0.27679	0.27980
0.0703	0.29012	0.29221	0.29532
0.0781	0.30353	0.30572	0.30896
0.0938	0.32627	0.32872	0.33202
0.1563	0.37095	0.37238	0.37555
0.2266	0.33075	0.32986	0.33235
0.2344	0.32235	0.32136	0.32374
0.5000	0.02526	0.02470	0.02527
0.8047	−0.31966	−0.31876	−0.31977
0.8594	−0.42665	−0.42620	−0.42653
0.9063	−0.51550	−0.51846	−0.52447
0.9453	−0.39188	−0.39433	−0.40618
0.9531	−0.33714	−0.33916	−0.35108
0.9609	−0.27669	−0.27879	−0.28961
0.9688	−0.21388	−0.21512	−0.22423
1.0000	0.00000	0.00000	0.00000

TABLE 4
Distribution of *U*-Velocity along Vertical Central Line with $M = 0.15$, $K = 0$

	Re = 100		Re = 400		Re = 1,000		Re = 2,000
y	Ghias	Present	Ghias	Present	Ghias	Present	Present
0.0000	0.0000	0.0000	0.0000	0.0000	0.0000	0.0000	0.0000
0.0547	−0.0372	−0.0373	−0.0819	−0.0813	−0.1811	−0.1771	−0.2712
0.0625	−0.0419	−0.0420	−0.0927	−0.0921	−0.2020	−0.1980	−0.2982
0.0703	−0.0477	−0.0467	−0.1034	−0.1028	−0.2222	−0.2185	−0.3232
0.1016	−0.0643	−0.0645	−0.1461	−0.1456	−0.2973	−0.2958	−0.3914
0.1719	−0.1015	−0.1020	−0.2430	−0.2432	−0.3829	−0.3847	−0.3530
0.2812	−0.1566	−0.1580	−0.3273	−0.3275	−0.2781	−0.2782	−0.2384
0.4531	−0.2109	−0.2131	−0.1712	−0.1705	−0.1065	−0.1071	−0.0834
0.5000	−0.2058	−0.2077	−0.1148	−0.1143	−0.0608	−0.0614	−0.0414
0.6172	−0.1364	−0.1367	0.0214	0.0216	0.0570	0.0566	0.0668
0.7344	0.0033	0.0053	0.1626	0.1625	0.1872	0.1868	0.1862
0.8516	0.2315	0.2349	0.2909	0.2905	0.3330	0.3333	0.3300
0.9531	0.6872	0.6896	0.5589	0.5591	0.4660	0.4675	0.4303
0.9609	0.7372	0.7392	0.6176	0.6176	0.5112	0.5124	0.4504
0.9688	0.7887	0.7903	0.6844	0.6844	0.5749	0.5758	0.4914
0.9766	0.8412	0.8424	0.7584	0.7582	0.6593	0.6596	0.5647

	Re = 3,200		Re = 5,000		Re = 7,500		Re = 10,000	
y	Ghias	Present	Ghias	Present	Ghias	Present	Ghias	Present
0.0000	0.0000	0.0000	0.0000	0.0000	0.0000	0.0000	0.0000	0.0000
0.0547	−0.3241	−0.3390	−0.4117	−0.4089	−0.4315	−0.4336	−0.4274	−0.4539
0.0625	−0.3534	−0.3692	−0.4290	−0.4270	−0.4359	−0.4343	−0.4254	−0.4617
0.0703	−0.3783	−0.3923	−0.4364	−0.4348	−0.4302	−0.4271	−0.4166	−0.4502
0.1016	−0.4193	−0.4174	−0.4044	−0.4014	−0.3832	−0.3794	−0.3800	−0.3778
0.1719	−0.3432	−0.3392	−0.3305	−0.3135	−0.3239	−0.3198	−0.3271	−0.2942
0.2812	−0.2443	−0.2357	−0.2286	−0.2065	−0.2318	−0.2189	−0.2319	−0.1834
0.4531	−0.0664	−0.0711	−0.0740	−0.0620	−0.0750	−0.0634	−0.0754	−0.0543
0.5000	−0.0427	−0.0273	−0.0304	−0.0260	−0.0380	−0.0254	−0.0311	−0.0211
0.6172	0.0716	0.0800	0.0818	0.0670	0.0834	0.0719	0.0834	0.0650
0.7344	0.1979	0.1920	0.2009	0.1768	0.2059	0.1924	0.2067	0.1623
0.8516	0.3468	0.3277	0.3356	0.3189	0.3423	0.3378	0.3464	0.3045
0.9531	0.4610	0.4385	0.4604	0.4560	0.4717	0.4698	0.4780	0.4634
0.9609	0.4655	0.4437	0.4599	0.4600	0.4732	0.4711	0.4807	0.4799
0.9688	0.4830	0.4614	0.4612	0.4614	0.4705	0.4708	0.4778	0.4721
0.9766	0.5324	0.5110	0.4822	0.4819	0.4724	0.4734	0.4722	0.4723
1.0000	1.0000	1.0000	1.0000	1.0000	1.0000	1.0000	1.0000	1.0000

for U and V velocities. According to Tables 4 and 5, the relative difference in the peak velocity between the BGK solution and Ghia's results is less than 5%.

3.2. *Effect of Boundary Condition*

Correct simulation of low-speed flow requires the implementation of appropriate boundary conditions. For incompressible Navier–Stokes equations, the energy equation is decoupled from continuity and momentum equations. In this case, the adherent condition (no slip) is used for the velocity boundary condition. Then, for pressure, Poisson's equation with the

TABLE 5
Distribution of V-Velocity along Horizontal Central Line with $K = 0$, $M = 0.15$

	Re = 100		Re = 400		Re = 1,000		Re = 2,000
x	Ghias	Present	Ghias	Present	Ghias	Present	Present
0.0000	0.0000	0.0000	0.0000	0.0000	0.0000	0.0000	0.0000
0.0625	0.0923	0.0932	0.1836	0.1830	0.2749	0.2768	0.3332
0.0703	0.1009	0.1019	0.1971	0.1965	0.2901	0.2922	0.3487
0.0781	0.1089	0.1100	0.2092	0.2086	0.3035	0.3057	0.3620
0.0938	0.1232	0.1244	0.2297	0.2291	0.3263	0.3286	0.3819
0.1563	0.1608	0.1625	0.2812	0.2810	0.3710	0.3724	0.3741
0.2266	0.1751	0.1773	0.3020	0.3018	0.3307	0.3300	0.2926
0.2344	0.1753	0.1775	0.3017	0.3015	0.3223	0.3214	0.2838
0.5000	0.0545	0.0561	0.0519	0.0513	0.0253	0.0247	0.0166
0.8047	−0.2453	−0.2517	−0.3860	−0.3861	−0.3197	−0.3188	−0.3011
0.8594	−0.2245	−0.2309	−0.4499	−0.4501	−0.4266	−0.4262	−0.3653
0.9063	−0.1691	−0.1743	−0.3383	−0.3821	−0.5155	−0.5185	−0.4768
0.9453	−0.1031	−0.1065	−0.2285	−0.2278	−0.3919	−0.3943	−0.5059
0.9531	−0.0886	−0.0915	−0.1925	−0.1918	−0.3371	−0.3392	−0.4620
0.9609	−0.0739	−0.0764	−0.1566	−0.1561	−0.2767	−0.2788	−0.3966
0.9688	−0.0591	−0.0609	−0.1215	−0.1207	−0.2139	−0.2151	−0.3137
1.0000	0.0000	0.0000	0.0000	0.0000	0.0000	0.0000	0.0000

	Re = 3,200		Re = 5,000		Re = 7,500		Re = 10,000	
x	Ghias	Present	Ghias	Present	Ghias	Present	Ghias	Present
0.0000	0.0000	0.0000	0.0000	0.0000	0.0000	0.0000	0.0000	0.0000
0.0625	0.3956	0.3810	0.4245	0.4221	0.4398	0.4402	0.4398	0.4365
0.0703	0.4092	0.3951	0.4333	0.4316	0.4403	0.4427	0.4373	0.4413
0.0781	0.4191	0.4055	0.4365	0.4353	0.4356	0.4379	0.4312	0.4375
0.0938	0.4277	0.4155	0.4295	0.4278	0.4182	0.4169	0.4149	0.4165
0.1563	0.3712	0.3640	0.3537	0.3449	0.3506	0.3327	0.3507	0.3279
0.2266	0.2903	0.2871	0.2807	0.2616	0.2812	0.2627	0.2800	0.2416
0.2344	0.2819	0.2791	0.2728	0.2529	0.2735	0.2554	0.2722	0.2326
0.5000	0.0100	0.0083	0.0094	0.0068	0.0082	0.0136	0.0083	0.0065
0.8047	−0.3118	−0.3003	−0.3002	−0.2807	−0.3045	−0.2869	−0.3072	−0.2649
0.8594	−0.3740	−0.3615	−0.3621	−0.3512	−0.3621	−0.3454	−0.3674	−0.3351
0.9063	−0.4431	−0.4318	−0.4144	−0.4117	−0.4105	−0.4013	−0.4150	−0.3974
0.9453	−0.5405	−0.5369	−0.5288	−0.5320	−0.4859	−0.4850	−0.4586	−0.4515
0.9531	−0.5236	−0.5220	−0.5541	−0.5571	−0.5235	−0.5245	−0.4910	−0.4897
0.9609	−0.4742	−0.4747	−0.5507	−0.5520	−0.5522	−0.5544	−0.5299	−0.5336
0.9688	−0.3902	−0.3906	−0.4977	−0.4956	−0.5386	−0.5436	−0.5430	−0.5512
1.0000	0.0000	0.0000	0.0000	0.0000	0.0000	0.0000	0.0000	0.0000

following boundary condition is usually solved,

$$\frac{\partial p}{\partial n} = \nu \frac{\partial^2 V_n}{\partial n^2}, \tag{21}$$

where n is the normal direction. For higher Reynolds numbers, the term on the right-hand side in the above equation can be ignored.

For the BGK scheme, the compressible flow equations are solved. Therefore, it is necessary to impose boundary conditions on velocity, density, and either pressure or temperature.

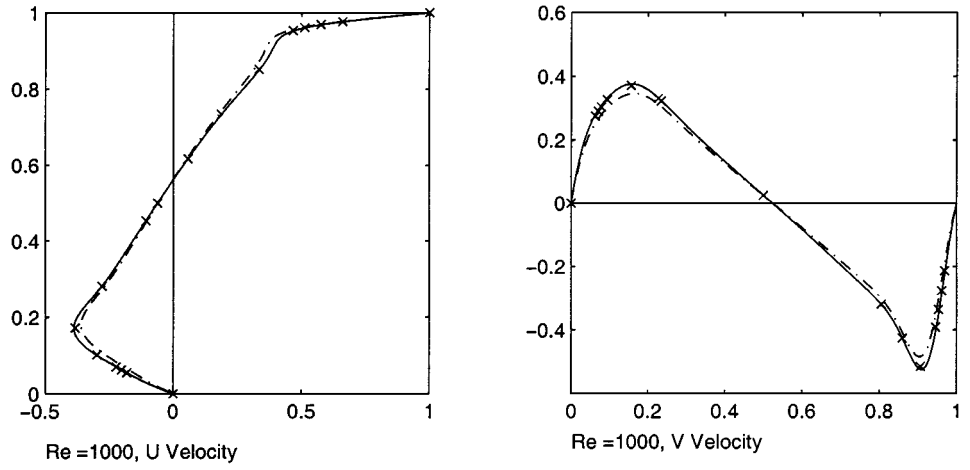

FIG. 4. Results of U and V velocities along vertical and horizontal lines by using isothermal and adiabatic boundary conditions. (×) Ghia's data; (—) $dT/dn = 0$; (- - -) $T =$ constant.

In the calculations, we use

$$\frac{\partial \rho}{\partial n} = 0,$$

for the density and adherence condition for the velocities at the wall. In addition, the following two temperature boundary conditions are tested in this paper:

$$\text{isothermal: } T = \text{constant} \qquad \text{and} \qquad \text{adiabatic: } \frac{\partial T}{\partial n} = 0.$$

Figure 4 plots the center line velocity distributions obtained from the BGK scheme by using the isothermal and adiabatic boundary conditions, and compared with Ghia's data. It is clear that the results of the isothermal boundary condition are slightly different from the results of the adiabatic boundary condition. The difference in the results can be explained from an energy transfer point of view. Assuming that temperature is constant at the wall, the BGK solution converges to a flow field whose steady-state temperature solution is constant everywhere in the flow domain. Yet, the viscous shear stresses continue to generate heat even when the flow reaches steady state. Hence, when the flow reaches its steady-state solution under the isothermal condition, all the heat generated by viscous forces is transferred out through the wall and the internal energy becomes constant. However, under the adiabatic boundary condition, the heat generated in the process of reaching steady state by the viscous forces in the upper surface is stored internally by the fluid. Hence, the temperature inside the cavity in the adiabatic case is higher than that in the isothermal case. As a result, the sound speed is higher in the formal case and it is equivalently more close to the incompressible case. Therefore, it is not surprising that the adiabatic boundary condition gives better results.

3.3. *Effect of Compressibility*

Incompressible flow is the limit case of the compressible flow when the Mach number M tends to zero. In the following, the effect of compressibility on the simulation results with $K = 0$ and under different Mach numbers is investigated. The BGK results for different Mach numbers and Ghia's data are compared in Table 6. From this table, it is obvious that the

TABLE 6
Comparison between Present Results (with Different M Number) and Ghia's Data

Distribution of U-velocity alone vertical central line

Y	$M=0.30$	$M=0.25$	$M=0.20$	$M=0.15$	$M=0.10$	$M=0.05$	Ghia
0.0000	0.0000	0.0000	0.0000	0.0000	0.0000	0.0000	0.0000
0.0547	−0.1788	−0.1784	−0.1779	−0.1771	−0.1767	−0.1747	−0.1811
0.0625	−0.1999	−0.1994	−0.1989	−0.1980	−0.1975	−0.1962	−0.2020
0.0703	−0.2204	−0.2199	−0.2194	−0.2185	−0.2180	−0.2176	−0.2222
0.1016	−0.2972	−0.2969	−0.2965	−0.2958	−0.2957	−0.2968	−0.2973
0.1719	−0.3834	−0.3840	−0.3844	−0.3847	−0.3849	−0.3828	−0.3829
0.2812	−0.2759	−0.2768	−0.2776	−0.2782	−0.2786	−0.2779	−0.2781
0.4531	−0.1058	−0.1063	−0.1067	−0.1071	−0.1076	−0.1058	−0.1065
0.5000	−0.0605	−0.0608	−0.0611	−0.0614	−0.0618	−0.0611	−0.0608
0.6172	0.0564	0.0565	0.0565	0.0566	0.0565	0.0560	0.0570
0.7344	0.1857	0.1862	0.1866	0.1868	0.1872	0.1871	0.1872
0.8516	0.3316	0.3324	0.3329	0.3333	0.3338	0.3329	0.3330
0.9531	0.4660	0.4668	0.4674	0.4675	0.4679	0.4705	0.4660
0.9609	0.5109	0.5116	0.5123	0.5124	0.5128	0.5150	0.5112
0.9688	0.5743	0.5750	0.5757	0.5758	0.5763	0.5785	0.5749
0.9766	0.6582	0.6589	0.6595	0.6596	0.6600	0.6623	0.6593
1.0000	1.0000	1.0000	1.0000	1.0000	1.0000	1.0000	1.0000

Distribution of V-velocity along horizontal central line

X	$M=0.30$	$M=0.25$	$M=0.20$	$M=0.15$	$M=0.10$	$M=0.05$	Ghia
0.0000	0.0000	0.0000	0.0000	0.0000	0.0000	0.0000	0.0000
0.0625	0.2763	0.2766	0.2768	0.2768	0.2794	0.2794	0.2749
0.0703	0.2918	0.2920	0.2922	0.2922	0.2948	0.2948	0.2901
0.0781	0.3053	0.3055	0.3057	0.3057	0.3086	0.3086	0.3035
0.0938	0.3282	0.3285	0.3287	0.3287	0.3323	0.3323	0.3263
0.1563	0.3711	0.3717	0.3722	0.3724	0.3738	0.3738	0.3710
0.2266	0.3279	0.3288	0.3295	0.3299	0.3290	0.3290	0.3307
0.2344	0.3193	0.3202	0.3209	0.3214	0.3209	0.3209	0.3223
0.5000	0.0243	0.0245	0.0246	0.0247	0.0226	0.0226	0.0253
0.8047	−0.3170	−0.3177	−0.3183	−0.3188	−0.3168	−0.3168	−0.3197
0.8594	−0.4245	−0.4252	−0.4258	−0.4262	−0.4249	−0.4249	−0.4266
0.9063	−0.5182	−0.5184	−0.5186	−0.5185	−0.5164	−0.5164	−0.5155
0.9453	−0.3972	−0.3966	−0.3957	−0.3943	−0.3909	−0.3909	−0.3919
0.9531	−0.3421	−0.3415	−0.3406	−0.3392	−0.3351	−0.3351	−0.3371
0.9609	−0.2816	−0.2810	−0.2801	−0.2788	−0.2736	−0.2736	−0.2767
0.9688	−0.2175	−0.2170	−0.2163	−0.2151	−0.2094	−0.2094	−0.2139
0.0000	0.0000	0.0000	0.0000	0.0000	0.0000	0.0000	0.0000

BGK solution uniformly approaches Ghia's solution as $M \to 0$. When $M = 0.15$, the relative difference in the peak velocity between the BGK solution and Ghia's results is less than 1%.

In the BGK scheme, another parameter that can influence the simulation results is the value of internal degree freedom K. Theoretically, if the fliud is incompressible the internal degree of freedom should take $K = 0$ because there is no energy exchange between external and internal molecular motion. Hence, the proper choice for the parameter K is zero (i.e., $K = 0$), which corresponds to $\gamma = 2$ and the coefficient of second viscosity becomes zero. Although $K = 0$ is the proper theoretical value, it is interesting to investigate the sensitivity of the BGK solution to this parameter. Table 7 lists the simulation results for different values

TABLE 7
Comparison between Present Results with Different K and Ghia's Data

Distribution of U-velocity along vertical central line

Y	$K=2/5$	$K=2/7$	$K=1/5$	$K=1/7$	$K=1/10$	$K=0$	Ghia
0.0000	0.0000	0.0000	0.0000	0.0000	0.0000	0.0000	0.0000
0.0547	−0.1717	−0.1772	−0.1771	−0.1771	−0.1771	−0.1771	−0.1811
0.0625	−0.1901	−0.1975	−0.1977	−0.1977	−0.1978	−0.1980	−0.2020
0.0703	−0.2076	−0.2173	−0.2176	−0.2178	−0.2181	−0.2185	−0.2222
0.1016	−0.2711	−0.2913	−0.2925	−0.2935	−0.2941	−0.2958	−0.2973
0.1719	−0.3472	−0.3769	−0.3790	−0.3805	−0.3817	−0.3847	−0.3829
0.2812	−0.2551	−0.2727	−0.2741	−0.2752	−0.2761	−0.2782	−0.2781
0.4531	−0.0938	−0.1039	−0.1047	−0.1054	−0.1059	−0.1071	−0.1065
0.5000	−0.0540	−0.0596	−0.0601	−0.0604	−0.0607	−0.0614	−0.0608
0.6172	0.0489	0.0548	0.0553	0.0556	0.0559	0.0566	0.0570
0.7344	0.1655	0.1820	0.1832	0.1841	0.1850	0.1868	0.1872
0.8516	0.2955	0.3252	0.3273	0.3288	0.3302	0.3333	0.3330
0.9531	0.4332	0.4606	0.4625	0.4638	0.4649	0.4675	0.4660
0.9609	0.4840	0.5064	0.5080	0.5092	0.5101	0.5124	0.5112
0.9688	0.5523	0.5708	0.5721	0.5731	0.5739	0.5758	0.5749
0.9766	0.6392	0.6557	0.6568	0.6575	0.6582	0.6596	0.6593
1.0000	1.0000	1.0000	1.0000	1.0000	1.0000	1.0000	1.0000

Distribution of V-velocity along horizontal central line

X	$K=2/5$	$K=2/7$	$K=1/5$	$K=1/7$	$K=1/10$	$K=0$	Ghia
0.0000	0.0000	0.0000	0.0000	0.0000	0.0000	0.0000	0.0000
0.0625	0.2683	0.2703	0.2721	0.2734	0.2743	0.2768	0.2749
0.0703	0.2832	0.2854	0.2872	0.2886	0.2896	0.2922	0.2901
0.0781	0.2962	0.2986	0.3005	0.3020	0.3031	0.3057	0.3035
0.0938	0.3184	0.3209	0.3230	0.3245	0.3257	0.3286	0.3263
0.1563	0.3616	0.3642	0.3664	0.3680	0.3693	0.3724	0.3710
0.2266	0.3232	0.3248	0.3261	0.3271	0.3280	0.3300	0.3307
0.2344	0.3150	0.3166	0.3177	0.3186	0.3195	0.3214	0.3223
0.5000	0.0251	0.0250	0.0249	0.0248	0.0248	0.0247	0.0253
0.8047	−0.3099	−0.3121	−0.3138	−0.3151	−0.3162	−0.3188	−0.3197
0.8594	−0.4193	−0.4211	−0.4224	−0.4234	−0.4243	−0.4262	−0.4266
0.9063	−0.5106	−0.5126	−0.5141	−0.5152	−0.5162	−0.5185	−0.5155
0.9453	−0.3878	−0.3894	−0.3906	−0.3916	−0.3925	−0.3943	−0.3919
0.9531	−0.3338	−0.3350	−0.3361	−0.3369	−0.3376	−0.3392	−0.3371
0.9609	−0.2746	−0.2756	−0.2764	−0.2770	−0.2776	−0.2788	−0.2767
0.9688	−0.2121	−0.2128	−0.2134	−0.2138	−0.2143	−0.2151	−0.2139
0.0000	0.0000	0.0000	0.0000	0.0000	0.0000	0.0000	0.0000

of K (i.e., different values of γ). It can be concluded that for $K \leq 1/5$ and $M \leq 0.15$, the numerical results from the compressible BGK scheme are nearly indistinguishable from the solution of the incompressible fluid equations, where the compressible error is indeed on the order of M^2.

It can be concluded here that the BGK solution properly models the incompressible equations because the overall divergence of velocity field is found to be very small in all cases. In fact, the divergence of the velocity field is on the order of 10^{-7} and remains nearly constant once steady state is achieved. Figure 5 shows maximum density fluctuation versus Mach number, the divergence of velocity field versus Mach number, and the divergence

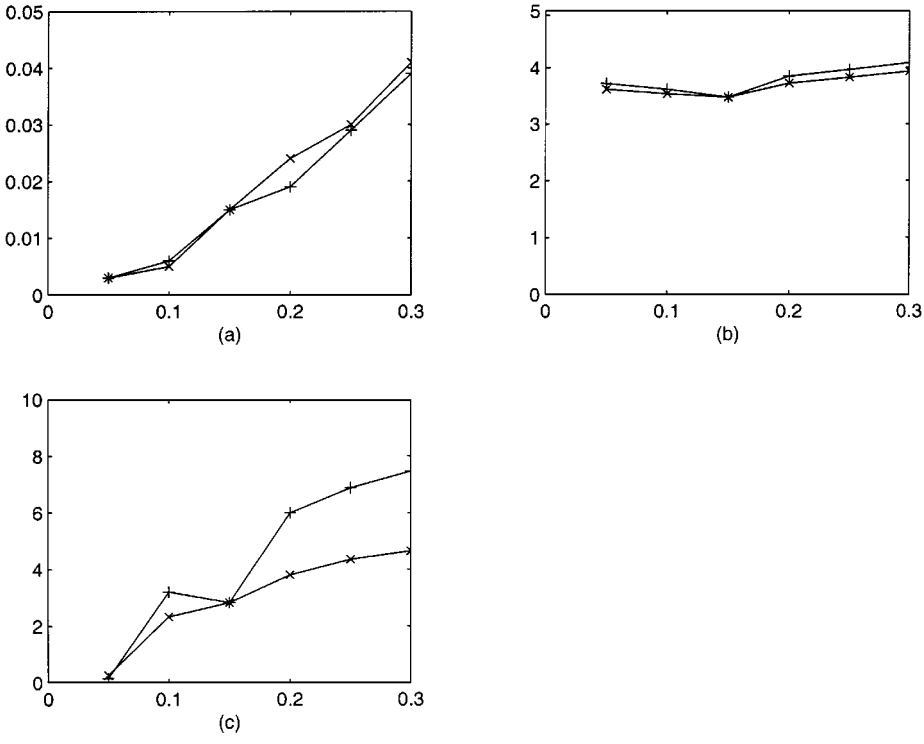

FIG. 5. Results with Re = 1000. (×) $K = 3.0$, (+) $K = 0.0$. (a) Maximum density fluctuation $\Delta\rho/\rho$ vs Mach number; (b) 10^7 Div(**U**) vs Mach number; (c) 10^8 Div(ρ**U**) vs Mach number.

of momentum versus Mach number. From these plots, it can be seen that the maximum density fluctuation and divergence of velocity and momentum are very small. Note that we are mainly concerned with the engineering application of the BGK method to the incompressible flow equations rather than with mathematical properties, such as divergence free solutions.

4. SIMULATION OF FLOW OVER A BACKWARD FACING STEP

In this section, the BGK scheme is applied to a backward facing step problem. This test case is chosen mainly because both the numerical and experimental data are available for the backward facing step problem [9]. In addition, this test case has also been used to study the lattice BGK method [3]. The geometry of the test case is the following:

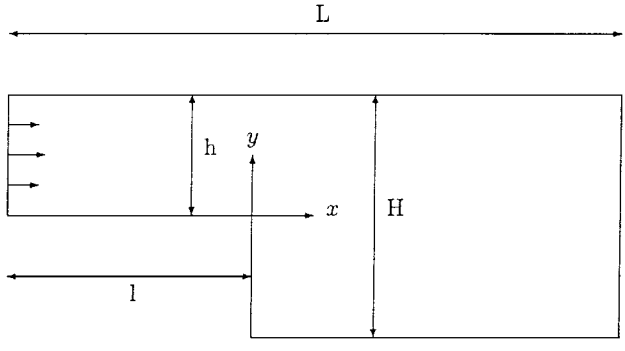

TABLE 8
Geometric Parameters in Three Cases

Case	Re	h	H	$h_s = H - h$	$U_{\max}$
1	50	2	3	1	7.23
2	150	2	3	1	21.7
3	150	2	4	2	10.8

Table 8 provides a summary of the three test cases performed in this paper. The numerical results from these three test cases are compared with experimental results in [9].

In the table, the Reynolds number is defined as $\mathrm{Re} = (H - h)U_{\max,\mathrm{entry}}/\nu$. According to the experiment, the viscous coefficient is defined as

$$\nu = [14.5 - 0.44 * (T^\circ - 20)]10^{-2}\ \mathrm{cm}^2/\mathrm{s},$$

where T° is the temperature and is equal to 20 in the experiment. The experimental data are described by Kueny in [9]. In the present simulation, the computational field is limited to the region bounded by $(-4 \le x/(H - h) \le 30$ and $-1 \le y/(H - h) \le h/(H - h)$. At the inlet, the velocity has a parabolic profile and the maximum horizontal velocity component has the magnitude 1.5. The density and pressure are set to be constant. At the wall, the no-slip boundary condition for velocity is used. In addition, the conditions for density and pressure at the wall are

$$\frac{\partial \rho}{\partial n} = 0, \qquad \frac{\partial p}{\partial n} = 0.$$

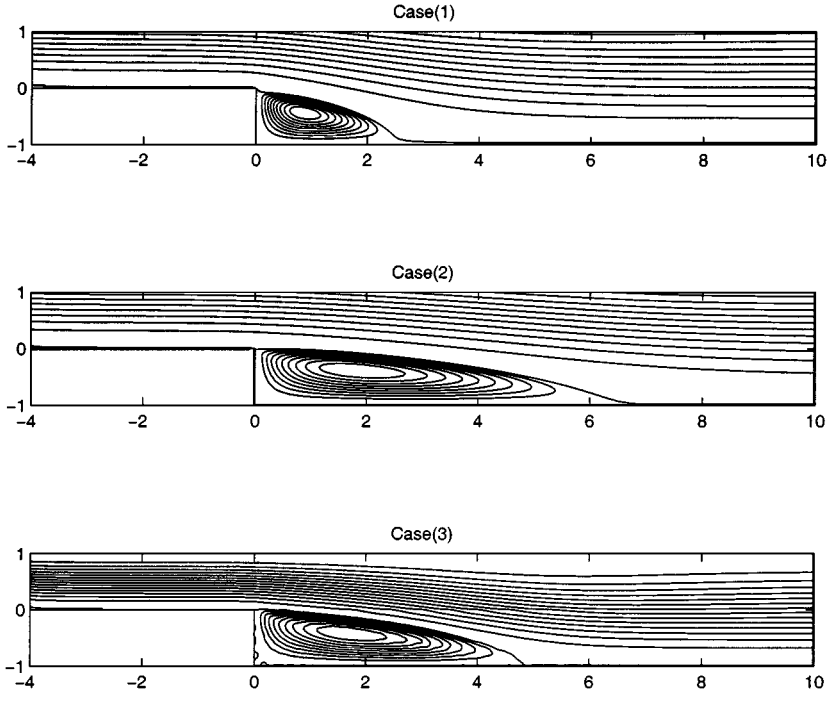

FIG. 6. Streamline distributions in three cases.

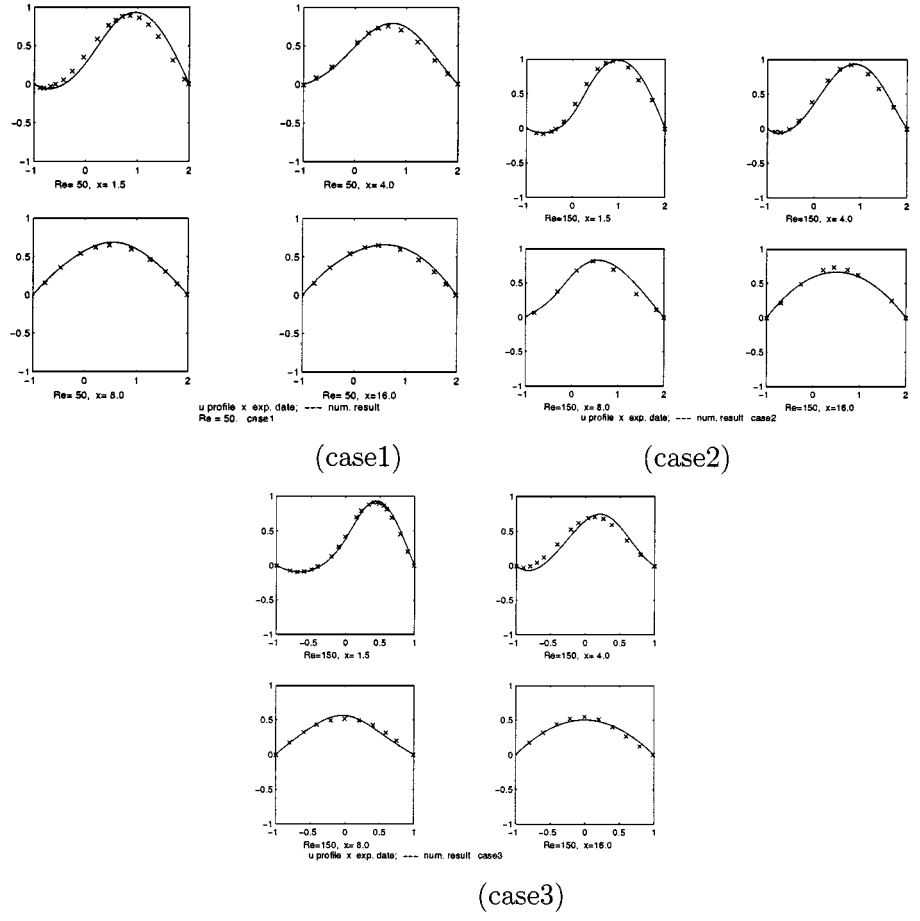

FIG. 7. Comparison of U-velocity profile at four different locations. ($\times$) Experimental data [9]; (—) present calculations.

At the outflow boundary, the free boundary condition in x-direction is used. That is,

$$\frac{\partial U}{\partial x}, \frac{\partial V}{\partial x}, \frac{\partial \rho}{\partial x}, \frac{\partial p}{\partial x} = 0.$$

The mesh used for cases 1 and 2 in Table 8 is 1202×152, and that for case 3 is 1202×102. Therefore, the grid size is uniform for all three cases, where $\Delta x = 0.03$ and $\Delta y = 0.02$. Also, $K = 0$, $M = 0.15$ are used in the current calculations. The numerical results of these three cases are shown in Figs. 6–8. These figures display (i) the structure of flow fields; (ii) the velocity profiles at x-locations of $1.5H - h$, $4H - h$, $8H - h$, and $16H - h$; (iii) the

TABLE 9
***x*-Coordinate of Reattachment Points**

	Case 1	Case 2	Case 3
Exp. [9]:	3	6	4.5
Num.:	3	6.3	4.8

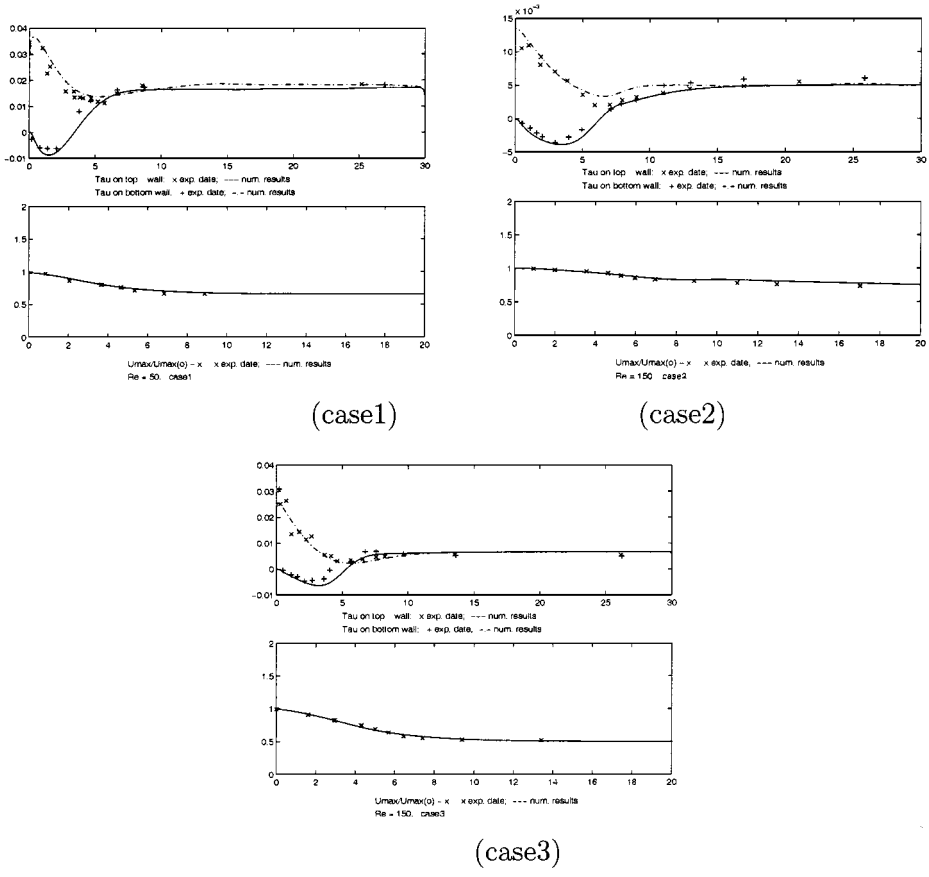

FIG. 8. Comparison of shear stress $\tau_{w,\text{top}}$, $\tau_{w,\text{bottom}}$ and $U_{\max}/U_{\text{mac}}(0)$ in the three cases. (×) Experimental data [9]; (—, - - -) present calculations.

distribution of the maximum velocity at different cross sections; and (vi) the shear stress on top and bottom walls along x-direction.

Similar to the lattice BGK method, there is a distinct difference in the locations of the reattachment points in our simulation results from the experimental data. The distance between the reattachment point and the backface is listed in Table 9. However, the velocity profile at fixed locations and the shear stress at the top and bottom are very close to the experimental data.

5. CONCLUSION

The BGK-based scheme is extended to the simulation of low-speed flow in the present paper. With $K = 0$, $M \leq 0.30$, the simulation results from compressible BGK code give an excellent agreement with the results from incompressible codes and experiments. This good agreement suggests that the proposed compressible BGK method can faithfully model incompressible flows when the Mach number is small. The main feature of the current approach that distinguishes it from incompressible codes is that there is no Poisson equation involved in the current method. In addition, unlike the lattice BGK method [8], the present scheme is an extension of the compressible BGK code [12] and uses a continuous phase

space rather than a fixed number of particle velocities. Hence, shocks and other discontinuities can naturally be calculated by these kinds of proposed kinetic schemes. Finally, the present method can be easily parallelized and extended to three dimensions. The drawback of the current approach is that the CFL condition is used for the determination of time step, which can be extremely small for the very small Mach number flow, and the pressure term could become stiff and generate numerical errors. So, for extremely subsonic flow, the adaptation of the preconditioning technique, which changes the sound speed numerically, will be helpful. However, in many engineering applications, it is not necessary to make M extremely small. As shown in this paper, the calculations with $M = 0.15$ give results almost identical to those from incompressible code. The two test cases in this paper have little change in the temperature distribution of the flow field. Actually, the largest error in the application of the compressible code to the incompressible flow simulation is attributable to the thermal effects. The ideal equation of state used in most compressible code will automatically generate a large density change if there are significant temperature variations. This related issue is discussed in [13].

APPENDIX: MOMENTS OF THE MAXWELLIAN DISTRIBUTION FUNCTION

In the gas-kinetic scheme, we need to evaluate moments of the Maxwellian distribution function with bounded and unbounded integration limits. Here, we list some general formulas.

First, we assume that the Maxwellian distribution for two dimensional flow is

$$g = \rho\left(\frac{\lambda}{\pi}\right)^{(K+2)/2} e^{-\lambda((u-U)^2+(v-V)^2+\xi^2)},$$

where ξ has K degrees of freedom. Then, by introducing the following notation for the moments of g,

$$\rho\langle\cdots\rangle = \int(\cdots)g\,du\,dv\,d\xi,$$

the general moment formula becomes

$$\langle u^n v^m \xi^l\rangle = \langle u^n\rangle\langle v^m\rangle\langle\xi^l\rangle,$$

where n, m are integers, and l is an even integer due to the symmetry in ξ-space. The moments of $\langle\xi^l\rangle$ are

$$\langle\xi^2\rangle = \left(\frac{K}{2\lambda}\right)$$
$$\langle\xi^4\rangle = \left(\frac{3K}{4\lambda^2} + \frac{K(K-1)}{4\lambda^2}\right).$$

The values of $\langle u^n\rangle$ depend on the integration limits. When the limits are from $-\infty$ to $+\infty$, we have

$$\langle u^0\rangle = 1$$
$$\langle u\rangle = U$$
$$\cdots$$
$$\langle u^{n+2}\rangle = U\langle u^{n+1}\rangle + \frac{n+1}{2\lambda}\langle u^n\rangle.$$

Similarly,

$$\begin{aligned} \langle v^0 \rangle &= 1 \\ \langle v \rangle &= V \\ &\cdots \\ \langle v^{n+2} \rangle &= V \langle v^{n+1} \rangle + \frac{n+1}{2\lambda} \langle v^n \rangle. \end{aligned}$$

ACKNOWLEDGMENTS

The authors acknowledge financial support from the Hong Kong Research Grant Cuncil through RGC97/98.HKUST6166/97P and RGC96/97.HKUST718/96E, and the National Science Foundation of China through the Climb Project.

REFERENCES

1. P. L. Bhatnagar, E. P. Gross, and M. Krook, A model for collision processes in gases. I. Small amplitude processes in charged and neutral one-component systems, *Phys. Rev.* **94**, 511 (1954).
2. S. Y. Chen and G. D. Doolen, Lattice Boltzmann method for fluid flows, *Ann. Rev. Fluid Mech.* (1998).
3. Y. Chen, H. Ohashi, and M. Akiyama, Simulation of laminar flow over a backward-facing step using the lattice BGK method, *JSME Int. J. Ser. B* **40**, 25 (1997).
4. A. J. Chorin, Numerical solution of the Navier–Stokes equations, *Math. Comput.* **22**, 745 (1968).
5. X. G. Deng and F. G. Zhuang, New methods for low Mach number flow calculations, in *The first Asian CFD Conference, Hong Kong, Jan. 16–19, 1995*.
6. P. M. Gresho, On the theory of semi-implicit projection methods for viscous incompressible flow and its implementation via finite element method that also introduces a nearly consistent mass matrix. Part 1: Theory; Part 2: Implementation, *Int. J. Num. Methods Fluids* **11**, 587 (1990).
7. U. Ghia, K. N. Ghia, and C. T. Shin, High-resolution for incompressible flow using the Navier–Stokes equations and a multigrid method, *J. Comput. Phys.* **48**, 387 (1982).
8. S. L. Hou, Q. S. Zou, S. Y. Chen, G. Doole, and A. C. Cogley, Simulation of cavity flow by the lattice Boltzmann method, *J. Comput. Phys.* **118**, 329 (1995).
9. K. Morgan, J. Periaux, and F. Thomasset, Analysis of laminar flow over a backward facing step, *Notes Numer. Fluid Mech.* **9**, 32 (1984).
10. E. Toro, *Riemann Solvers and Numerical Methods for Fluid Dynamics* (Springer-Verlag, Berlin/New York, 1997).
11. K. Xu, *Numerical Hydrodynamics from Gas-Kinetic Theory* (Ph.D. thesis, Columbia University, 1993).
12. K. Xu, Gas-kinetic schemes for unsteady compressible flow simulation, in *CFD Lecture Series* (von Karman Institute for Fluid Dynamics, 1998).
13. K. Xu and S. H. Lui, Rayleigh–Benard simulation using gas-kinetic BGK scheme in the incompressible limit, *Phys. Rev. E*, in press.
14. K. Xu, L. Martinelli, and A. Jameson, Gas-kinetic finite volume methods, flux-vector splitting and artificial diffusion, *J. Comput. Phys.* **120**, 48 (1995).
15. Z. J. Wang, A fast flux-splitting for all speed flow, in *15th International Conference on Numerical Methods in Fluid Dynamics, 1996*, p. 141.